JOURNAL OF PROPULSION AND POWER
Vol. 20, No. 6, November–December 2004

Rotor-Bearing Analysis for Turbomachinery Single- and Dual-Rotor Systems

Hsiao-Wei D. Chiang* and Chih-Neng Hsu†
National Tsing Hua University, Hsinchu 300, Taiwan, Republic of China
and
Shun-Hsu Tu‡
Industrial Technology Research Institute, Hsinchu 310, Taiwan, Republic of China

Finite element analysis models were developed to investigate the dynamic characteristics of single- and dual-rotor-bearing turbomachinery systems. When an inertial coordinate system was used, the dynamic models of the rotor-bearing systems included gyroscopic moments, rotary inertias, and bending and shear deformations. The models were analyzed to predict the natural frequencies, to produce critical speed maps, and to estimate the bearing stiffnesses. These rotor-bearing system analyses were then applied to both single-rotor and dual-rotor system applications. In the single-rotor system application, a small turbojet engine and its rotor components were used as a basis for the model. Both theoretical and experimental analyses were used to study this engine rotor-bearing system. Modal testing and a dynamic engine test were used to verify the analytical results, including the predicted critical speed map and the bearing stiffnesses. Very good agreement was found between the analyses and the test data. In the dual-rotor application, the effects of the speed ratio of the high-speed to low-speed shafts of the dual-rotor system on the critical speeds was studied. It was demonstrated that this speed ratio could be used as one of the dual-rotor system design parameters. Finally, it was noted that the interrotor bearing stiffness between the high-speed and the low-speed shafts of the dual-rotor system affected the mode shapes of the shafts within the system, in addition to the rotor system critical speeds.

Nomenclature

A	=	element area
$[C]$	=	damping matrix
EI	=	bending stiffness per unit of curvature
$\{F\}$	=	external force vector
G	=	shear modulus
$[G]$	=	gyroscopic matrix
I	=	moment of inertia
$[K]$	=	stiffness matrix
ℓ	=	element length
$[M]$	=	mass matrix
$\{q\}$	=	displacement vector
S_r	=	shear factor
λ	=	eigenvalue, $\alpha \pm i\omega$
ρ	=	density
$[\phi]$	=	total system eigenvector matrix
$\{\phi\}$	=	amplitude displacement vector
Ω	=	rotational speed
ω_j	=	jth natural frequency
ω_0	=	natural frequency
ω_1	=	rotor 1 speed
ω_2	=	rotor 2 speed

Subscripts

A	=	axial load
B	=	bending
K	=	stiffness
R	=	rotational
T	=	translational
x	=	coordinate of x direction
y	=	coordinate of y direction
1	=	point 1 position
2	=	point 2 position

Superscripts

b	=	bearing
C	=	casing
d	=	disk
e	=	element
(r)	=	order number
S	=	system
(1), (2), (3), . . . , (n)	=	first-, second-, third-, . . . , nth-order number

I. Introduction

FINITE element methods have been used in rotordynamic analyses since 1970. In the early days, only the bending vibrations under rotor linear displacement conditions were considered. Later, rotor models were improved to include rotatory inertia, gyroscopic moments, axial loads, internal and external damping, and shear deformations. Hibner[1] used a unique transfer matrix method applied to an idealized equivalent engine system for predicting vibratory responses that accounted for nonlinear viscous damping effects. Glasgow and Nelson[2] applied a common mode synthesis method and showed that a significant reduction in the size of the problem is achieved when analyzing the stability of a dual-rotor system. Li and Hamilton[3] applied a simplified transfer matrix method with squeeze film dampers on two-spool-rotor systems. Huang[4] developed a transfer matrix impedance coupling method to predict frequency responses of mutiple-rotor systems. Zeng and Hu[5] used a gyroscopic mode synthesis technique for multishaft-rotor-bearing casing systems. Gupta et al.[6] used a modified transfer matrix method to study the energy distributions in a multispool rotor system. However, because of the transfer matrix method's assumptions,[7] it sometimes resulted in numerical instability problems or in missing-root problems.[8]

Received 15 June 2003; revision received 13 April 2004; accepted for publication 26 April 2004.

*Associate Professor, Department of Power Mechanical Engineering.
†Ph.D. Candidate, Department of Power Mechanical Engineering.
‡Engineer, Center for Aerospace and Systems Technology.

The analyses presented herein are based on the methods used by Nelson and Mcvaugh,[9] Nelson,[10] and Lalanne and Ferraris.[11] The finite element rotor-bearing system models were established using inertial coordinate systems. The models were used to predict natural frequencies, critical-speed maps, and bearing stiffnesses. Based on the Lagrangian formulation, this general model of continuous rotor-bearing systems was established, and included gyroscopic moments, rotary inertias, and bending and shear deformations. The rotor-bearing system analyses were then applied to a single-rotor application and a dual-rotor application.

For the single-rotor application, a small turbojet engine was used as the basis for the finite element model. This engine produces 12 lbf (5.4432 kgf) of thrust and was developed for unmanned aerial vehicle (UAV) applications. In recent years, the growing interest in remote control airplanes has created a new marketplace for scaled-down operational aircraft (including UAVs) and small turbojet engines. The small turbojet engine[12] used in this study utilizes existing turbocharger rotor components. This design takes advantage of readily made rotor systems that are available commercially through the automobile turbocharger market. The high-strength and temperature resistant construction of these rotors provides a low-cost compressor and turbine system.

The small turbojet engine rotor design originally called for a critical speed margin of at least 15∼20% as a guideline[13] to prevent excessive vibrations, which may in turn damage the rotor system. To meet these requirements, the rotor-bearing system analysis was developed to investigate the characteristics of the rotor design. Modal testing and dynamic engine testing were used to verify the analytical results, including critical speed maps and bearing stiffnesses.

Multiple rotor designs were first introduced in the 1960s. Turbofan engines require multiple speeds for efficiency and stall margin, and as a result, it has become very common for turbofan engines to have dual- or even triple-rotor system designs. On these types of engines, it is essential to use multiple compressor stages on multiple rotors and to drive each rotor by a separate turbine. This arrangement provides dual-spool coupling by introducing an interrotor bearing between the high-speed and the low-speed shafts of the dual-rotor system. However, the interrotor bearing also becomes a source of coupling vibrations between the two shafts.[14]

II. Rotor-Bearing System Model

A typical flexible rotor-bearing system model consists of discrete disks, rotor segments with distributed masses and elastic characteristics, and discrete bearings. Figure 1 shows such a system, along with an x–y coordinate system used to describe the system motion.

A. Element Divisions and Structural Nodal Displacements

The rotor system can be divided into rigid disks, rotor segments, and linear bearing supports as shown in Fig. 2. Also shown are nodal displacements in an inertial coordinate system, where

$$\{q\} = \{x_1, y_1, \theta_{x1}, \theta_{y1}, x_2, y_2, \theta_{x2}, \theta_{y2}\} \tag{1}$$

and where x_1, y_1, θ_{x1}, and θ_{y1} represent node 1's displacements and x_2, y_2, θ_{x2}, and θ_{y2} represent node 2's displacements.

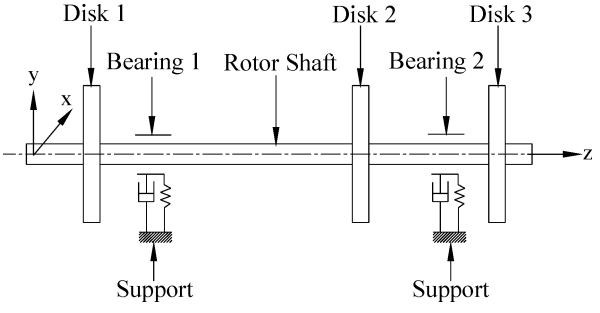

Fig. 1 Typical rotor-bearing system.

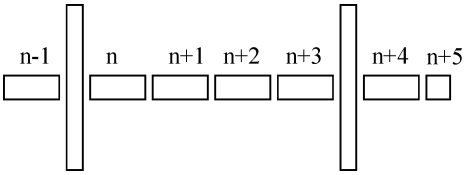

a) Rotor elements

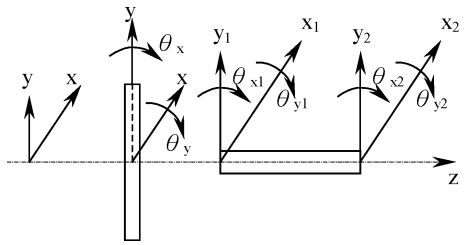

b) Rotor and disk local coordinate system

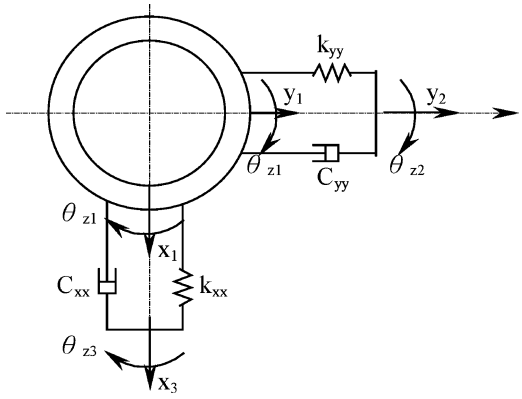

c) Support elements

Fig. 2 Rotor-bearing system elements.

B. Component Equations

In this section, a rigid-disk equation of motion is developed for the rotor-bearing system using a Lagrangian formulation.

1. Rigid Disk

The equation for the rigid disk is

$$\left(\left[M_T^d\right] + \left[M_R^d\right]\right)\{\ddot{q}^d\} - \Omega[G^d]\{\dot{q}^d\} = \{F^d\} \tag{2}$$

where

$$\left[M_T^d\right] = \begin{bmatrix} m_d & 0 & 0 & 0 \\ 0 & m_d & 0 & 0 \\ 0 & 0 & 0 & 0 \\ 0 & 0 & 0 & 0 \end{bmatrix}, \qquad \left[M_R^d\right] = \begin{bmatrix} 0 & 0 & 0 & 0 \\ 0 & 0 & 0 & 0 \\ 0 & 0 & I_d & 0 \\ 0 & 0 & 0 & I_d \end{bmatrix}$$

$$[G^d] = \begin{bmatrix} 0 & 0 & 0 & 0 \\ 0 & 0 & 0 & 0 \\ 0 & 0 & 0 & -I_P \\ 0 & 0 & I_P & 0 \end{bmatrix}$$

2. Finite Rotor Elements

The elements are

$$\left(\left[M_T^e\right] + \left[M_R^e\right]\right)\{\ddot{q}^e\} - \Omega[G^e]\{\dot{q}^e\} + \left[K_B^e\right]\{q^e\} = \{F^e\} \tag{3}$$

In Eq. (3), $[M_T^e]$, $[M_R^e]$, $[G^e]$, and $[K_B^e]$ are given in the Appendix.

3. Linear Bearings

The bearings are

$$-[C^b]\{\dot{q}^b\} - [K^b]\{q^b\} = \{F^b\} \tag{4}$$

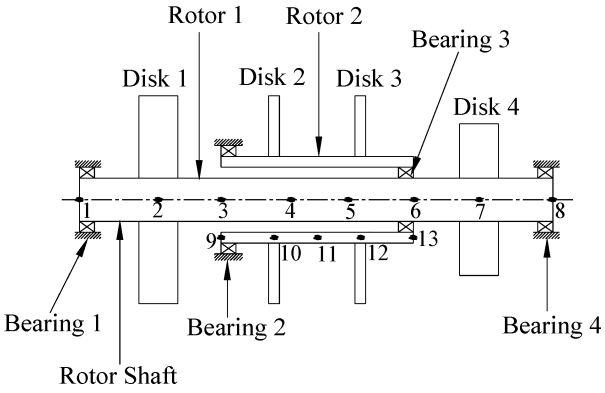

Fig. 3 Dual-rotor system model.

where

$$[C^b] = \begin{bmatrix} C_{xx} & C_{xy} & 0 & 0 \\ C_{xy} & C_{yy} & 0 & 0 \\ 0 & 0 & 0 & 0 \\ 0 & 0 & 0 & 0 \end{bmatrix}, \qquad [K^b] = \begin{bmatrix} K_{xx} & K_{xy} & 0 & 0 \\ K_{xy} & K_{yy} & 0 & 0 \\ 0 & 0 & 0 & 0 \\ 0 & 0 & 0 & 0 \end{bmatrix}$$

4. Dual-Rotor Interrotor Bearing

The interrotor bearing is

$$-[C^{sb}]\{\dot{q}^{sb}\} - [K^{sb}]\{q^{sb}\} = \{F^{sb}\} \tag{5}$$

If the bearing is located between rotor 1, i node, and rotor 2, j node, as shown in Fig. 3 (bearing 3), then

$$[C^{sb}] = \begin{array}{c} \begin{matrix} {\scriptstyle 4i-3} & {\scriptstyle 4i-2} & {\scriptstyle 4j-3} & {\scriptstyle 4j-2} \end{matrix} \\ \left[\begin{array}{cc|cc} C_{xx} & C_{xy} & -C_{xx} & -C_{xy} \\ C_{xy} & C_{yy} & -C_{xy} & -C_{yy} \\ \hline -C_{xx} & -C_{xy} & C_{xx} & C_{xy} \\ -C_{xy} & -C_{yy} & C_{xy} & C_{yy} \end{array}\right] \begin{matrix} {\scriptstyle 4i-3} \\ {\scriptstyle 4i-2} \\ {\scriptstyle 4j-3} \\ {\scriptstyle 4j-2} \end{matrix} \end{array}$$

$$[K^{sb}] = \begin{array}{c} \begin{matrix} {\scriptstyle 4i-3} & {\scriptstyle 4i-2} & {\scriptstyle 4j-3} & {\scriptstyle 4j-2} \end{matrix} \\ \left[\begin{array}{cc|cc} K_{xx} & K_{xy} & -K_{xx} & -K_{xy} \\ K_{xy} & K_{yy} & -K_{xy} & -K_{yy} \\ \hline -K_{xx} & -K_{xy} & K_{xx} & K_{xy} \\ -K_{xy} & -K_{yy} & K_{xy} & K_{yy} \end{array}\right] \begin{matrix} {\scriptstyle 4i-3} \\ {\scriptstyle 4i-2} \\ {\scriptstyle 4j-3} \\ {\scriptstyle 4j-2} \end{matrix} \end{array}$$

C. System Equation of Motion

1. Single-Rotor-Bearing System

The assembled system equation of motion, consisting of component equations of Eqs. (2–4) is of the form

$$[M]\{\ddot{q}^S\} + ([C] + \Omega[G])\{\dot{q}^S\} + [K]\{q^S\} = \{F^S\} \tag{6}$$

where

$$\{q^S\} = \{x_1, y_1, \theta_{x1}, \theta_{y1}, \ldots, x_n, y_n, \theta_{xn}, \theta_{yn}\}^T$$

2. Dual-Rotor-Bearing System

For rotor 1,

$$[M_1]\left\{\ddot{q}_1^S\right\} + ([C_1] + \Omega_1[G_1])\left\{\dot{q}_1^S\right\} + [K_1]\left\{q_1^S\right\} = \left\{F_1^S\right\} \tag{7}$$

For rotor 2,

$$[M_2]\left\{\ddot{q}_2^S\right\} + ([C_2] + \Omega_2[G_2])\left\{\dot{q}_2^S\right\} + [K_2]\left\{q_2^S\right\} = \left\{F_2^S\right\} \tag{8}$$

When Eqs. (7) and (8) are combined, the equation of motion for the dual-rotor-bearing system and casing can be obtained,

$$\left[\begin{array}{c|c} M^S & 0 \\ \hline 0 & M^C \end{array}\right]\left\{\begin{matrix} \ddot{q}^S \\ \ddot{q}^C \end{matrix}\right\} + \left[\begin{array}{c|c} [C] + \Omega_1[G_1] + \Omega_2[G_2] & 0 \\ \hline 0 & 0 \end{array}\right]\left\{\begin{matrix} \dot{q}^S \\ \dot{q}^C \end{matrix}\right\} + \left[\begin{array}{c|c} K^{SS} & K^{SC} \\ \hline K^{CS} & K^{CC} \end{array}\right]\left\{\begin{matrix} q^S \\ q^C \end{matrix}\right\} = \left\{\begin{matrix} F^S \\ F^C \end{matrix}\right\} \tag{9}$$

where the vectors $\boldsymbol{q}^S$ and $\boldsymbol{q}^C$ represent the displacements of the rotor system and flexible casing, respectively. In this paper, the casing effects are assumed to be negligible.

III. Solutions of Rotor-Bearing System

To calculate the critical speeds for the system, the following homogeneous equation needs to be solved:

$$[M^S]\{\ddot{q}^S\} + [C^S]\{\dot{q}^S\} + [K^S]\{q^S\} = \{0\} \tag{10}$$

Equation (10) is an eigenvalue solution problem. In structural dynamics, there are many ways to solve large-scale sparse matrix eigenvalue problems. However, most of the time, these solution approaches are only useful for cases with small damping and symmetrical matrices. Because the effects of gyroscopic moments, anisotropic bearings, and material damping are included herein, the damping and stiffness matrices become nonsymmetric and dependent on speed. Consequently, the equation needs to be solved in a different way, as follows.

The second-order homogeneous equation (10) is reduced into $2n$ first-order differential equations. A $2n$-order column vector $\{X\}$,

$$\{X\} = \begin{Bmatrix} \dot{q} \\ q \end{Bmatrix} \tag{11}$$

is used so that Eq. (10) can be expressed as

$$\begin{bmatrix} \mathbf{0} & M \\ M & C \end{bmatrix}\begin{Bmatrix} \ddot{q} \\ \dot{q} \end{Bmatrix} + \begin{bmatrix} -M & \mathbf{0} \\ \mathbf{0} & K \end{bmatrix}\begin{Bmatrix} \dot{q} \\ q \end{Bmatrix} = \begin{Bmatrix} \mathbf{0} \\ \mathbf{0} \end{Bmatrix} \tag{12}$$

Equation (12) can be simplified into

$$[A]\{\dot{X}\} + [B]\{X\} = \{0\} \tag{13}$$

By the assumption that

$$\{X\} = \{\phi\}e^{\lambda t}, \qquad \{\dot{X}\} = \lambda\{\phi\}e^{\lambda t} \tag{14}$$

Eq. (14) can be substituted into Eq. (13) to obtain

$$(\lambda A + B)\{\phi\} = 0 \tag{15}$$

Using QR[15] or Lanczos methods,[15] the eigenvalues and eigenvectors for Eq. (15) can be solved. Because Eq. (12) contains the damping term C, the eigenvalues and eigenvectors are complex numbers. From the eigenvalue, $\lambda_K = \alpha_K \pm i\omega_K$, the damped critical speeds and the speeds corresponding to the onset of whirl can be determined.

IV. Single-Rotor Application: Simulation and Test Results

A small turbojet engine was used for the single-rotor application. Both modal testing and dynamic engine testing were used to verify the analytical results. Figure 4 shows the small turbojet engine and the rotor-bearing system, which consists of a rotor shaft, a compressor, a turbine, a spacer, a bearing inner ring, and an oil ring. The total length of the rotor system is approximately 171 mm. The subsystems of the engine include a starting system, a fuel control system, and an oil lubrication system.

The analyses of this application included the tasks described as follows.

A. Free–Free Modal Testing

In this study, a hammer impact experimental method is used. A free–free support boundary condition was assumed for the modal testing, which implies that the test object is unconstrained. To satisfy this assumption, the test object was suspended using an elastic string to simulate the free support condition. An impact hammer was then used with a load cell to apply the impact force. An accelerometer on the test object recorded the response due to the impact. Both the impact force and the response are amplified and input to a fast Fourier transform analyzer to obtain a frequency response function.

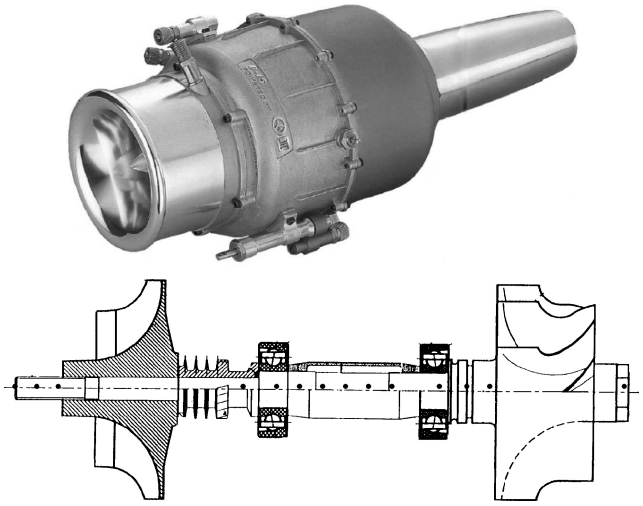

Fig. 4 Turbojet engine and rotor-bearing system.

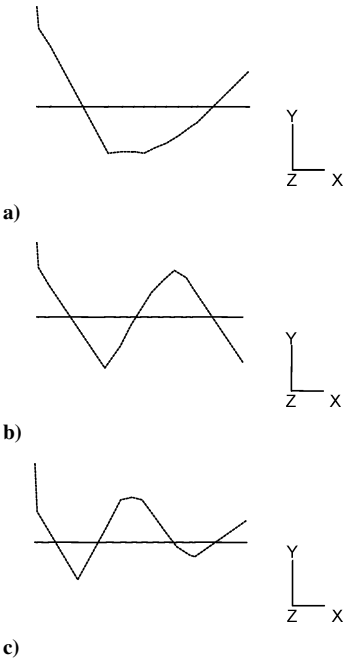

Fig. 5 Turbojet rotor free–free support modal testing results, def. 0.0 Hz: a) first mode, 1467 Hz, b) second mode, 3693 Hz, and c) third mode, 8002 Hz.

Through the use of a routine identification procedure, the mode shape related parameters could be determined.

Figure 5 shows the first three mode frequencies and the mode shapes from the test results of the free–free modal testing.

B. Finite Element Analysis for Free–Free Model

With use of Eq. (6), the first three mode frequencies and mode shapes were solved, producing the results shown in Fig. 6. Comparison of the test results from the modal testing, as presented in Fig. 5, with the predicted mode shapes and frequencies, shows that the frequency differences are within 3% for the first three modes, as indicated in Table 1. Comparison of the mode shapes also shows very good agreement. From the foregoing results, it is concluded that the analyses correlate quite well with the free–free test data.

C. Critical Speed Map Calculation

When the damping term in Eq. (6) is neglected and the equation to use a rotating coordinate system is transformed, the number of degrees of freedom for the system can be reduced by one-half. In this way, the critical speed map can be obtained directly as shown in Fig. 7. This map is based on the assumptions of equal stiffness for both the front and the rear bearings. As shown in Fig. 7, the rotor-bearing system with elastic supports has first and second critical speeds that increase as the stiffness increase, whereas the third-order critical speed is almost constant. However, with a rigid-support condition, the first two critical speeds remain almost constant as the stiffness is increased, whereas the third critical speed increases with the increase in the stiffness due to gyroscopic effects.

Table 1 Small turbojet engine free support natural frequencies

	Order		
Frequency	1st	2nd	3rd
Modal testing, Hz	1467	3693	8002
Mathematic model, Hz	1441.4	3591.4	8160.7
Difference, %	2.0	3.0	2.0

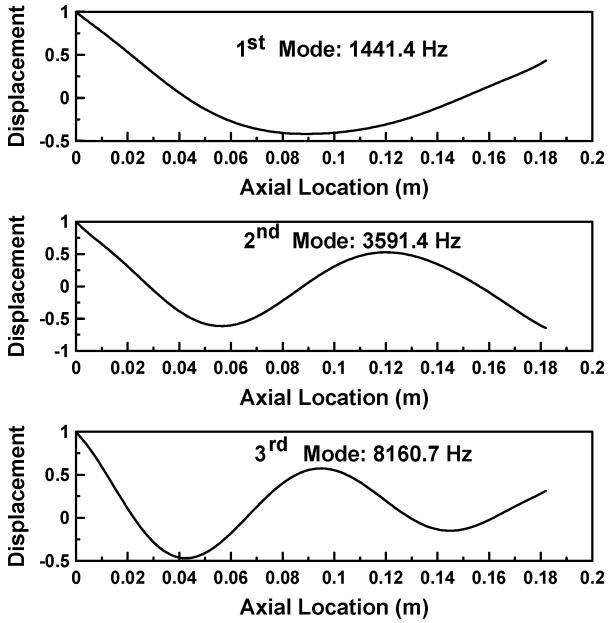

Fig. 6 Turbojet free–free support calculated results, P15 mode shape.

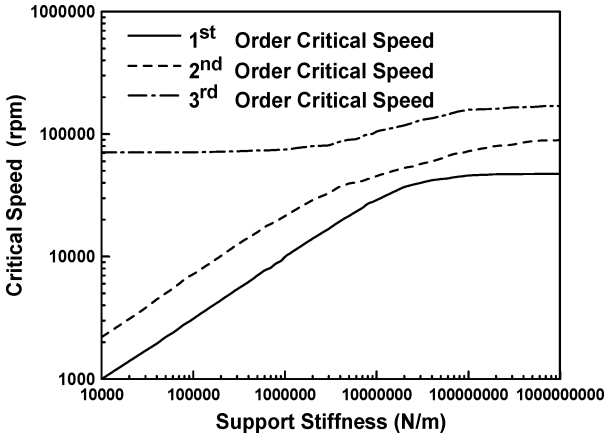

Fig. 7 Turbojet critical speed map.

D. Turbojet Engine Dynamic Testing

A turbojet engine dynamic testing facility was established for this study. This facility was composed of the turbojet engine, a test stand, instrumentation, and a personal computer-based data acquisition system. An accelerometer was mounted on the engine to measure the engine critical speeds. Figure 8 shows the order tracking plot results

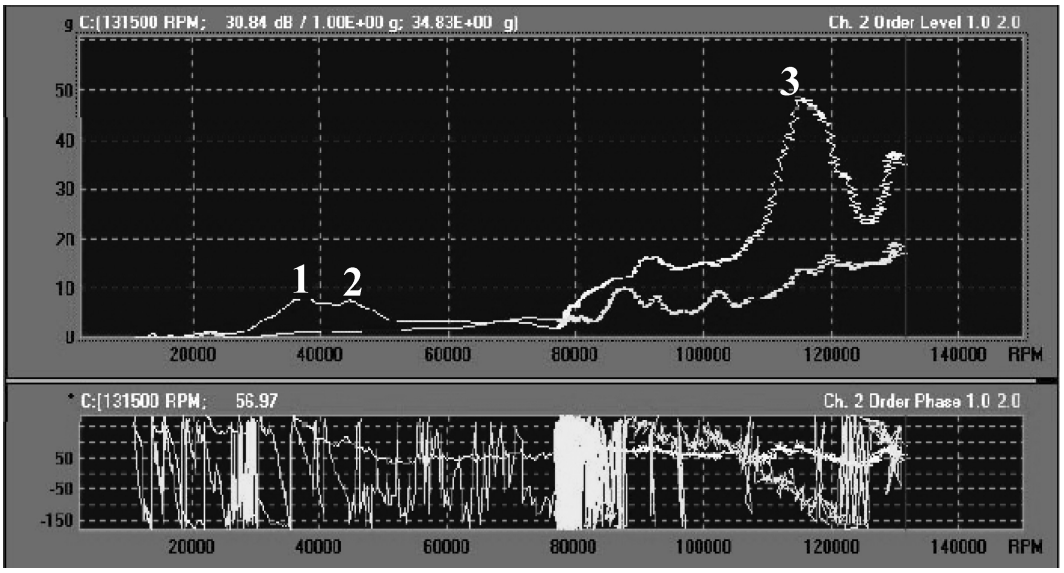

Fig. 8 Turbojet dynamic testing order-tracking results.

Table 2 Small turbojet engine critical speeds[a]

	Order		
Speed	1st	2nd	3rd
Full engine test, rpm	35,556	46,032	117,140
Mathematic model, rpm	33,629	48,900	116,390
Difference, %	5.0	6.0	1.0

[a]Front bearing stiffness 1.6×10^7 N/m and back bearing stiffness 1.5×10^7 N/m.

from the engine dynamic testing. The first three critical speeds of 35,556, 46,032, and 117,140 rpm were obtained from the test results shown in Fig. 8. When the critical speed map results (Fig. 7) are compared with the results from engine dynamic testing, both the front and the rear bearing stiffness can be roughly estimated in the range 1×10^7–2×10^7 N/m.

E. Bearing Stiffness Matching Optimizations

The front and the rear bearing stiffnesses are used as optimization parameters to match the critical speed experimental value ω_{ei} (order i). The initial values and ranges of the bearing stiffnesses can be obtained using Fig. 7 (critical speed map) as a reference. When iterations of Eq. (12) are used, the bearing stiffness matching optimizations can be solved as

$$\min E = \sum_{i}^{3} \frac{\omega_{ei}^2 - \omega_{ci}^2}{\omega_{ei}^2} \tag{16}$$

where ω_{ei} is the critical speed test result and ω_{ci} the critical speed calculated result where $i = 1, 2, 3$.

The calculated results give a front bearing stiffness of 1.6×10^7 N/m and a rear bearing stiffness of 1.5×10^7 N/m, which result in corresponding critical speeds of 33,629, 48,900, and 116,390 rpm. Very good agreement was obtained with the experimental results, with the calculated differences below 6%, as indicated in Table 2. There are three critical speeds within the engine operation range of $0 \sim 140{,}000$ rpm. Therefore, the engine operation close to the critical speeds should be avoided to prevent bearing damage. If the single-rotor support design could be modified to a soft support ($K < 10^6$ N/m), then a comfortable speed margin could be maintained between the operating speed (135,000 rpm) and the third-order critical speed.

V. Dual-Rotor Application: Simulation Results

There are two possible modes of operation in a dual-rotor system. One is with both rotors corotating in the same direction and the other with the rotors counter rotating with respect to each other. In this paper, the typical case of corotation is considered.

Table 3 Nodal coordinates for the dual rotor system

Node	Axial distance, cm	Node	Axial distance, cm	Node	Axial distance, cm
1	0	6	40.64	11	27.94
2	7.62	7	45.72	12	35.56
3	15.875	8	50.8	13	40.64
4	24.13	9	15.24		
5	32.385	10	20.32		

Table 4 Disk data

	Disk			
Property	1	2	3	4
Mass, kg	10.51	7.01	3.5	7.01
I_{DX} kg · m^2	4.295×10^{-2}	2.145×10^{-2}	1.355×10^{-2}	3.39×10^{-2}
I_{DY}, kg · m^2	8.59×10^{-2}	4.29×10^{-2}	2.71×10^{-2}	6.78×10^{-2}

Table 5 Bearing stiffnesses

Bearing	$K_{xx} = K_{yy}$, N/m
1	2.63×10^7
2	1.75×10^7
3	8.75×10^6
4	1.75×10^7

Figure 3 shows an undamped dual rotor-bearing system provided by Ref. 11, with its nodal coordinates listed in Table 3. The data on the dual rotor-bearing system are as follows for rotor speed relation $\omega_2 = 1.5\omega_1$, where ω_1 is rotor 1 speed (with rotor 1 diameter = 30.5 mm) and ω_2 is rotor 2 speed (with inner diameter = 50.8 mm and outer diameter = 60.9 mm). Table 4 lists the data for the four disks shown in Fig. 3. With the assumption that the bearing stiffness is symmetrical (no cross stiffness), the data for the four bearings are provided in Table 5.

Because the dual-rotor system has two different rotor speeds, and the interrotor bearing causes the coupling of the two rotors, the critical speed calculations are much more complex than for the single-rotor system. Especially, the interrotor bearing stiffness between the high-speed and the low-speed shafts of the dual-rotor system can affect the mode shapes of the two shafts within the system, in addition to the rotor system critical speeds.

Table 6 Critical speeds of the dual rotor system for rotor 1 operating at a fixed speed

Rotor 1 speed, rpm	Critical speed, rpm			Rotor 1 speed, rpm	Critical speed, rpm		
	First mode	Second mode	Third mode		First mode	Second mode	Third mode
0	6,115	12,031	17,738	15,000	9,041	12,385	17,970
1,000	6,385	12,065	17,804	16,000	9,145	12,401	17,973
2,000	6,650	12,097	17,845	17,000	9,240	12,416	17,975
3,000	6,907	12,127	17,873	18,000	9,329	12,431	17,977
4,000	7,156	12,155	17,894	19,000	9,411	12,445	17,979
5,000	7,392	12,181	17,909	20,000	9,487	12,458	17,981
6,000	7,615	12,206	17,921	21,000	9,557	12,471	17,983
7,000	7,825	12,230	17,931	22,000	9,623	12,483	17,985
8,000	8,022	12,253	17,939	23,000	9,684	12,495	17,986
9,000	8,204	12,275	17,945	24,000	9,740	12,506	17,987
10,000	8,373	12,295	17,951	25,000	9,793	12,516	17,989
11,000	8,529	12,315	17,956	26,000	9,843	12,527	17,990
12,000	8,673	12,334	17,960	27,000	9,889	12,538	17,991
13,000	8,806	12,352	17,964	28,000	9,933	12,547	17,992
14,000	8,928	12,369	17,967	29,000	9,974	12,557	17,993

Table 7 Critical speeds of the dual rotor system for rotor 2 operating at a fixed speed

Rotor 2 speed, rpm	Critical speed, rpm			Rotor 2 speed, rpm	Critical speed, rpm		
	First mode	Second mode	Third mode		First mode	Second mode	Third mode
0	7,579	12,113	17,091	15,000	8,323	12,378	17,887
1,000	7,641	12,135	17,095	16,000	8,359	12,391	17,919
2,000	7,702	12,156	17,179	17,000	8,395	12,404	17,950
3,000	7,760	12,177	17,257	18,000	8,429	12,417	17,979
4,000	7,817	12,197	17,332	19,000	8,462	12,429	18,006
5,000	7,872	12,216	17,401	20,000	8,494	12,440	18,031
6,000	7,925	12,235	17,466	21,000	8,524	12,452	18,055
7,000	7,976	12,253	17,527	22,000	8,554	12,463	18,078
8,000	8,025	12,270	17,583	23,000	8,583	12,473	18,099
9,000	8,072	12,287	17,636	24,000	8,610	12,483	18,119
10,000	8,118	12,304	17,685	25,000	8,636	12,494	18,139
11,000	8,162	12,320	17,731	26,000	8,662	12,503	18,157
12,000	8,204	12,335	17,774	27,000	8,687	12,512	18,174
13,000	8,245	12,350	17,814	28,000	8,711	12,521	18,190
14,000	8,285	12,364	17,852	29,000	8,734	12,530	18,206

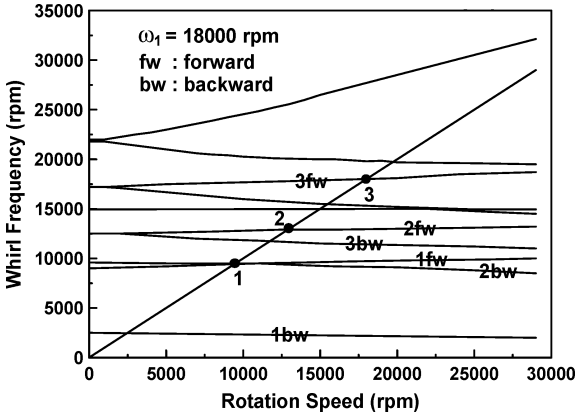

Fig. 9 Campbell diagram of dual-rotor critical speeds at ω_1 = 18,000 rpm.

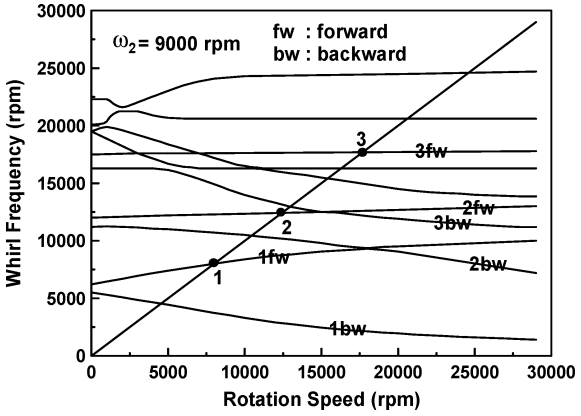

Fig. 10 Campbell diagram of dual-rotor critical speeds at ω_2 = 9000 rpm.

In this paper, the dual-rotor-system critical speed analyses included the following four tasks.

A. Task A

1) Apply Eqs. (9) and (13) with rotor 1 held at a constant speed ω_1 while varying the speed of rotor 2, ω_2. From the Campbell diagram, the corresponding critical speeds can be found as shown in Fig. 9, and these are listed in Table 6.

2) In a similar manner, with rotor 2 held at a constant speed ω_1, the speed of rotor 1 is varied, ω_1. The corresponding critical speeds from the Campbell diagram are shown in Fig. 10 and are also listed in Table 7.

3) Combining Tables 6 and 7, the dual rotor critical speed map can be obtained as shown in Fig. 11. Given the dual-rotor speed relation curve ($\omega_2 = 1.5\omega_1$), the first five critical speeds can be found from the crossing points as follows: First critical speed $(\omega_1; \omega_2)_1 = (4915; 7372)$, second critical speed $(\omega_1; \omega_2)_2 = (8171; 12{,}256)$, third critical speed $(\omega_1; \omega_2)_3 = (8218; 12{,}317)$, fourth critical speed $(\omega_1; \omega_2)_4 = (11{,}973; 17{,}960)$, and fifth critical speed $(\omega_1; \omega_2)_5 = (12{,}424; 18{,}636)$.

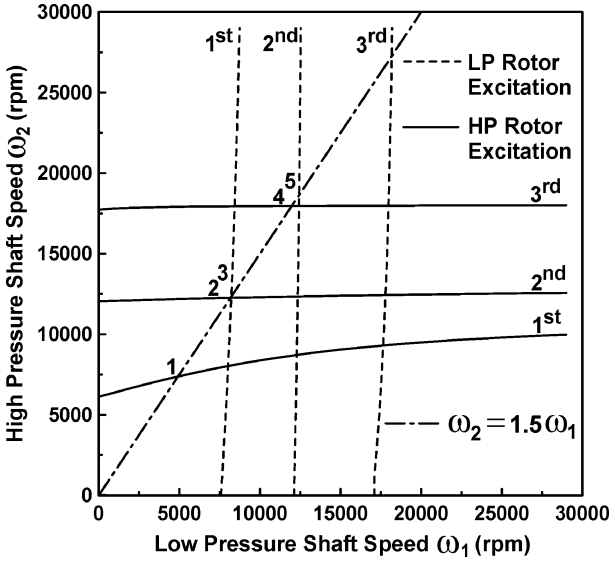

Fig. 11 Dual-rotor critical speed map from task A.

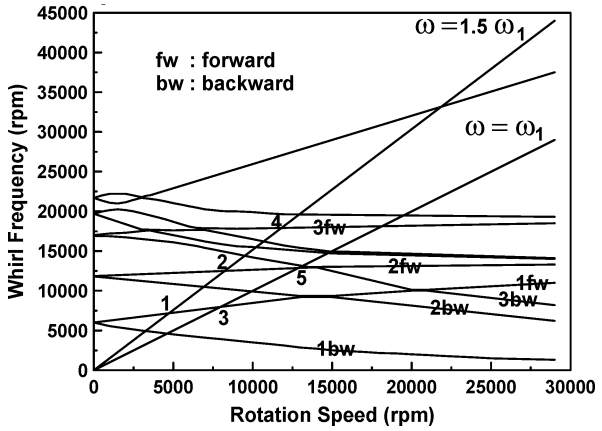

Fig. 12 Campbell diagram of task B rotor critical speed map.

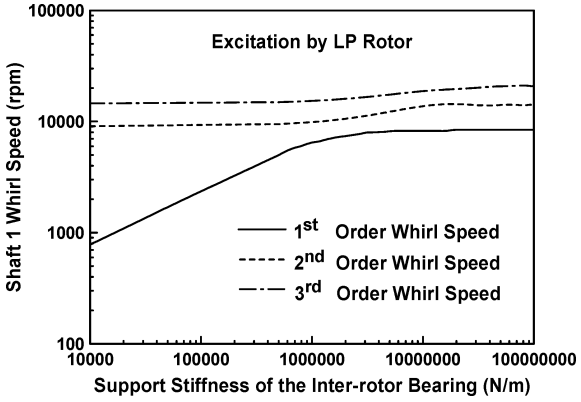

Fig. 13 Task C critical speed map for rotor 1.

This method can be used for linear or nonlinear dual-rotor speed relations. As shown in Fig. 11, both rotor 1 and rotor 2 critical speeds increase as the dual-rotor speed increases.

B. Task B

If the dual-rotor rotational speeds are in simple multiple relations, as in the preceding case ($\omega_2 = 1.5\omega_1$), Eqs. (9) and (13) can be solved directly using the Campbell diagram calculations to obtain the system critical speeds, as shown in Fig. 12. Consequently, the results are identical as those given in task A.

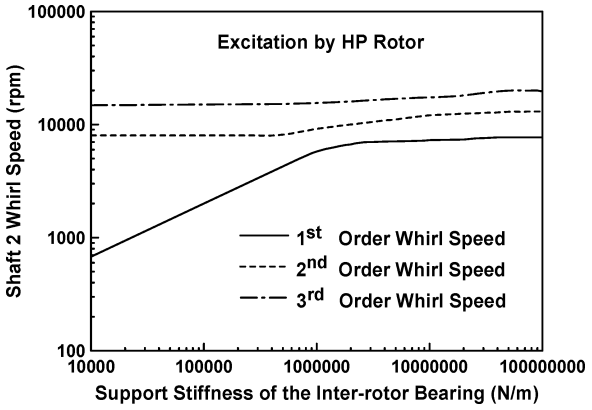

Fig. 14 Task C critical speed map for rotor 2.

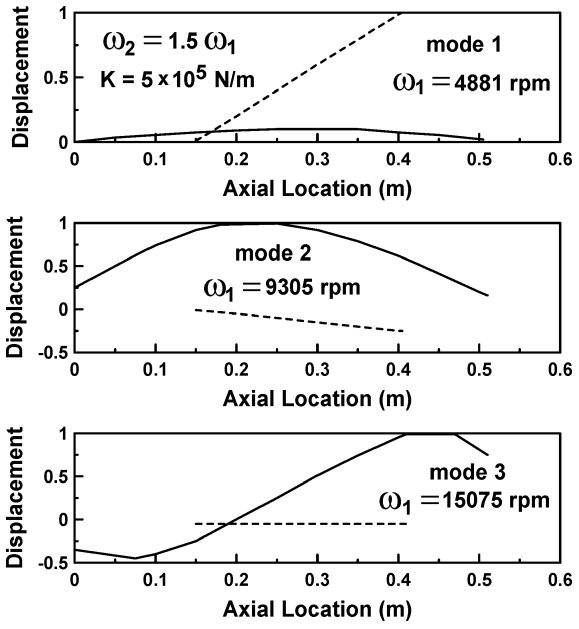

Fig. 15 Task D rotor mode shape with $K = 5 \times 10^5$ N/m due to rotor 1 excitations, spin ω_1/whirl = 1: ——, rotor 1 and - - - -, rotor 2.

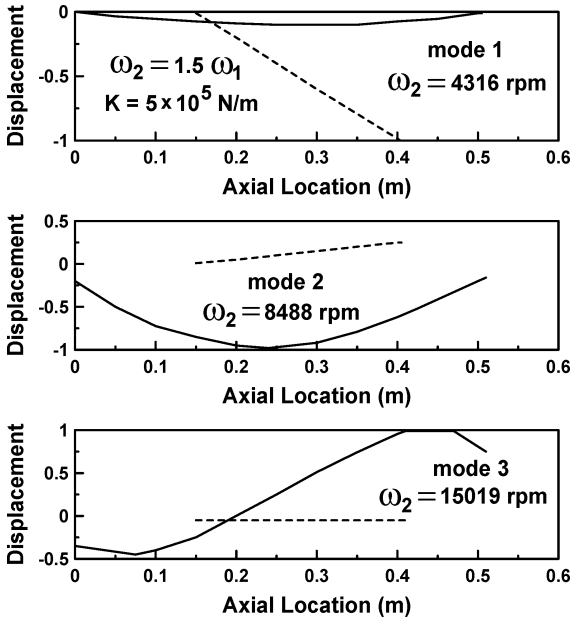

Fig. 16 Task D rotor mode shape with $K = 5 \times 10^5$ N/m due to rotor 2 excitations, spin ω_2/whirl = 1: ——, rotor 1 and - - - -, rotor 2.

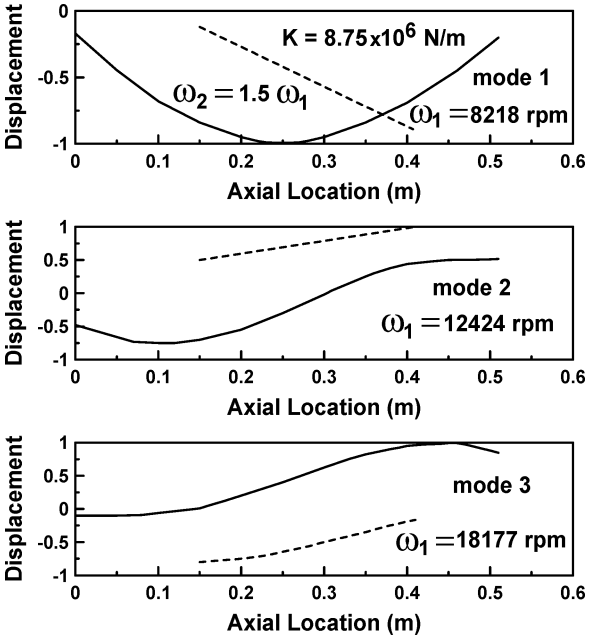

Fig. 17 Task D rotor mode shape with $K = 8.75 \times 10^6$ N/m due to rotor 1 excitations, spin ω_1/whirl = 1: ——, rotor 1 and - - - -, rotor 2.

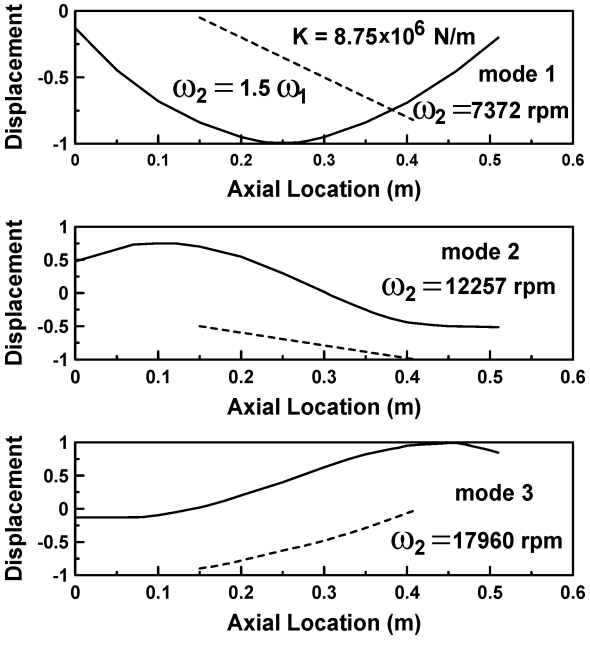

Fig. 18 Task D rotor mode shape with $K = 8.75 \times 10^6$ N/m due to rotor 2 excitations, spin ω_2/whirl = 1: ——, rotor 1 and - - - -, rotor 2.

C. Task C

In task A and task B, the dual-rotor-system critical speed calculations can be very complex, lengthy, and inefficient. The bearing stiffness was found to be one of the key parameters in critical speed design. Similar to the single-rotor undamped system, Eq. (9) can be converted into a rotating coordinate system. The number of degrees of freedom for the system can then be reduced by one-half. Furthermore, with use of simple multiple dual-rotor speed relations ($\omega_2 = 1.5\omega_1$), the interrotor bearing stiffness can be assumed to be a variable to obtain the critical speed map as shown in Figs. 13 and 14. The corresponding interrotor bearing stiffness is 8.76×10^6 N/m, and the critical speed results are in agreement with both tasks A and B. This demonstrates that using the interrotor bearing stiffness as a variable is an efficient method to calculate the dual-rotor system critical speeds.

D. Task D

As shown in Figs. 13 and 14, the critical speeds are dependent on the interrotor bearing stiffness. In high-speed rotating machinery, the rotor mode shapes can affect the rotor system stability. In Figs. 15–18, the rotor 1 and rotor 2 mode shapes are shown for the interrotor bearing stiffness of 5×10^5 and 8.75×10^6 N/m. In the case of the 5×10^5-N/m bearing stiffness, both the first- and second-rotor-system mode shapes are linear. Consequently, this demonstrates that the rotor system will not have instabilities caused by internal damping.

VI. Conclusions

A systematic theoretical analysis was developed to investigate the dynamic characteristics of single- and dual-rotor-bearing turbomachinery systems. A general model of continuous rotor-bearing systems was established based on the Lagrangian formulation, with gyroscopic moments, rotary inertias, and bending and shear deformations included within the model. This rotor-bearing system model was then used in a single-rotor-system application and a dual-rotor system application.

In the single-rotor-system application, a small turbojet engine was used to compare finite element single-rotor-bearing system analysis with modal testing results. The comparison demonstrated very good agreement. Critical speed map calculations, with bearing stiffnesses matching optimizations, also show very good agreement with the engine dynamic testing results.

In the dual-rotor-system application, the effects of the speed ratio on the critical speeds were studied. The dual-rotor speed ratio can affect the critical speeds. Consequently, it is one of the key design parameters for dual-rotor systems. It was noted that the interrotor bearing stiffness between the high-speed and the low-speed rotor not only affects the critical speeds, but also affects the mode shapes of the system. Finally, with use of the interrotor bearing stiffness as a variable, an efficient method was demonstrated to calculate the dual-rotor critical speeds. This approach can be used as a system design tool to define quickly the key parameters, including shaft dimensions, bearing locations, and bearing stiffnesses.

Appendix: Finite Rotor Element Matrices

$$\left[M_T^e\right] = \frac{\rho A \ell}{420(1+\Phi)^2} \begin{bmatrix} m_1 & & & & & & & \\ 0 & m_1 & & & & & & \\ 0 & -m_2\ell & m_5\ell^2 & & & \text{symm} & & \\ m_2\ell & 0 & 0 & m_5\ell^2 & & & & \\ m_3 & 0 & 0 & m_4\ell & m_1 & & & \\ 0 & m_3 & -m_4\ell & 0 & 0 & m_1 & & \\ 0 & m_4\ell & -m_6\ell^2 & 0 & 0 & m_2\ell & m_5\ell^2 & \\ -m_4\ell & 0 & 0 & -m_6\ell^2 & -m_2\ell & 0 & 0 & m_5\ell^2 \end{bmatrix}$$

$$\left[M_R^e\right] = \frac{\rho I}{30(1+\Phi)^2}\begin{bmatrix} m_7 & & & & & & & \\ 0 & m_7 & & & & & & \\ 0 & -m_8\ell & m_9\ell^2 & & & \text{symm} & & \\ m_8\ell & 0 & 0 & m_9\ell^2 & & & & \\ -m_7 & 0 & 0 & -m_8\ell & m_7 & & & \\ 0 & -m_7 & -m_8\ell & 0 & 0 & m_7 & & \\ 0 & -m_8\ell & -m_{10}\ell^2 & 0 & 0 & m_8\ell & m_9\ell^2 & \\ m_8\ell & 0 & 0 & -m_{10}\ell^2 & -m_8\ell & 0 & 0 & m_9\ell^2 \end{bmatrix}$$

$$[G^e] = \frac{\rho I}{15\ell(1+\Phi)^2}\begin{bmatrix} 0 & & & & & & & \\ m_7 & 0 & & & & & & \\ -m_{8\ell} & 0 & 0 & & & \text{symm} & & \\ 0 & -m_8\ell & m_9\ell^2 & 0 & & & & \\ 0 & m_7 & -m_8\ell & 0 & 0 & & & \\ -m_7 & 0 & 0 & -m_8\ell & m_7 & 0 & & \\ -m_8\ell & 0 & 0 & m_{10}\ell^2 & m_8\ell & 0 & 0 & \\ 0 & -m_8 & -m_{10}\ell & 0 & 0 & m_8\ell & m_9\ell & 0 \end{bmatrix}$$

$$\left[K_B^e\right] = \frac{EI}{\ell^3(1+\Phi)}\begin{bmatrix} 12 & & & & & & & \\ 0 & 12 & & & & & & \\ 0 & -6\ell & (4+\Phi)\ell^2 & & & \text{symm} & & \\ 6\ell & 0 & 0 & (4+\Phi)\ell^2 & & & & \\ -12 & 0 & 0 & -6\ell & 12 & & & \\ 0 & -12 & 6\ell & 0 & 0 & 12 & & \\ 0 & -6\ell & 2\ell^2 & 0 & 0 & 6\ell & (4+\Phi)\ell^2 & \\ 6\ell & 0 & 0 & (2-\Phi)\ell^2 & -6\ell & 0 & 0 & (4+\Phi)\ell^2 \end{bmatrix}$$

where

$$m_1 = 156 + 294\Phi + 140\Phi^2, \qquad m_2 = 22 + 38.5\Phi + 17.5\Phi^2$$

$$m_3 = 54 + 126\Phi + 70\Phi^2, \qquad m_4 = 13 + 31.5\Phi + 17.5\Phi^2$$

$$m_5 = 4 + 7\Phi + 3.5\Phi^2, \qquad m_6 = 3 + 7\Phi + 3.5\Phi^2$$

$$m_7 = 36, \qquad m_8 = 3 - 15\Phi, \qquad m_9 = 4 + 5\Phi + 10\Phi^2$$

$$m_{10} = 1 + 5\Phi - 5\Phi^2, \qquad \Phi = 12EI/GS_r\ell^2$$

where S_r is the shear factor.

Acknowledgments

The authors would like to thank Royce Lin and Aling Lai of the Thunder Tiger Corporation, for their valuable assistance during the preparation of this paper. Special thanks are due to Richard Lord, General Manager of PTEC Corporation, for his final revision of the paper.

References

[1]Hibner, D. H., "Dynamic Response of Viscous-Damped Multi-Shaft Jet Engines," *Journal of Aircraft*, Vol. 12, No. 4, 1975, pp. 305–312.

[2]Glasgow, D. A., and Nelson, H. D., "Stability Analysis of Rotor Bearing Systems Using Component Mode Synthesis," American Society of Mechanical Engineers, Paper 79-DET-63, Sept. 1979.

[3]Li, Q., and Hamilton, J. F., "Investigation of the Transient Response of a Dual-Rotor System with Inter-Rotor Squeeze Film Damper," *Journal of Engineering for Gas Turbines and Power*, Vol. 108, No. 4, 1986, pp. 613–618.

[4]Huang, T., "The Transfer Matrix Impedance Coupling Method for the Eigen Solutions of Multi-Spool Rotor Systems," *Modal Testing and Analysis*, DE-Vol. 3, American Society of Mechanical Engineers, New York, 1987, pp. 71–76.

[5]Zheng, Z. C., and Hu, Y., "The Dynamic Analysis of a Multi-Shaft Rotor-Bearing-Case System," *Vibration in Rotating Machinery*, Institute of Mechanical Engineers Conference Publication, Professional Engineering Publishing Limited, London, UK, 1988, pp. 607–614.

[6]Gupta, K. D., Gupta, K., and Athre, K., "Stability Analysis of Dual Rotor System by Extended Transfer Matrix Method," American Society of Mechanical Engineers, Paper 89-GT-194, June 1989.

[7]Kazao, Y., and Gunter, E. J., "Dynamics of Multi-Spool Gas Turbines Using the Matrix Transfer Method Theory," *International Journal of Turbo and Jet Engines*, Vol. 6, No. 2, 1989, pp. 153–161.

[8]Peduzzi, A., "Simulation of Advanced Engine Lubrication and Rotor Dynamics Systems Rig Design and Fabrication," AIAA Paper 83-1133, June 1983.

[9]Nelson, H. D., and Mcvaugh, J. M., "The Dynamics of Rotor-Bearing Systems Using Finite Elements," *Journal of Engineering for Industry*, Vol. 98, Ser. B, No. 2, 1976, pp. 593–600.

[10]Nelson, H. D., "A Finite Rotating Shaft Element Using Timoshenko Beam Theory," *Journal of Mechanical Design*, Vol. 102, No. 4, 1980, pp. 793–803.

[11]Lalanne, M., and Ferraris, G., *Rotordynamics Prediction in Engineering*, 1st ed., Wiley, New York, 1990, pp. 86–88.

[12]Chiang, H. W. D., Hsu, C. N., Lai, A., and Lin, R., "An Investigation of Steady and Dynamic Performances of a Small Turbojet Engine," American Society of Mechanical Engineers, Paper GT-2002-30577, June 2002.

[13]Chiang, H. W. D., Hsu, C. N., Jeng, W., Tu, S. H., and Li, W. C., "A Microturbine Rotor-Bearing System Analysis," American Society of Mechanical Engineers, Paper GT-2002-30316, June 2002.

[14]Chiang, H. W. D., Hsu, C. N., Jeng, W., Tu, S. H., and Li, W. C., "Turbomachinery Dual Rotor-Bearing System Analysis," American Society of Mechanical Engineers, Paper GT-2002-30315, June 2002.

[15]Cheung, Y. K., and Leung, A. Y. T., Finite Element Methods in Dynamics, Science Press, Beijing/New York/Hong Kong and Kluwer Academic Publishers, Dordrecht/Boston/London, 1991, pp. 146–205.

[16]Tu, S. H., Cheng, K., Li, W. C., and Hsiung, T. P., "The Calculation of Critical Speeds by FEM for a Dual Rotor-Bearing System of Aero Engines," *Proceedings of the 2001 CIROC/CSCA/AASRC Joint Conference*, Yuan Ze Univ. Publications, Taoyuan, Taiwan, R.O.C., 2001, pp. AA533–540.